

Endothelial Reprogramming Stimulated by Oncostatin M Promotes Inflammation and Tumorigenesis in *VHL*-Deficient Kidney Tissue

Hieu-Huy Nguyen-Tran¹, Thi-Ngoc Nguyen¹, Chen-Yun Chen¹, and Tien Hsu^{1,2,3}

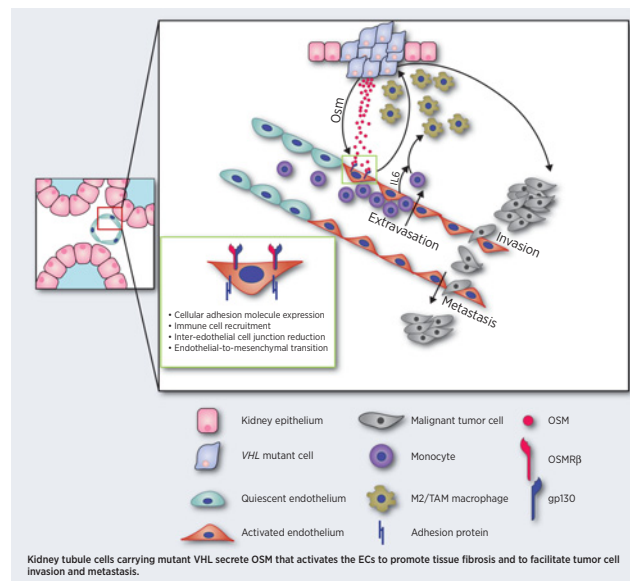


ABSTRACT

Clear-cell renal cell carcinoma (ccRCC) is the most prevalent subtype of renal cell carcinoma (RCC), and its progression has been linked to chronic inflammation. About 70% of the ccRCC cases are associated with inactivation of the von Hippel–Lindau (*VHL*) tumor-suppressor gene. However, it is still not clear how mutations in *VHL*, encoding the substrate-recognition subunit of an E3 ubiquitin ligase that targets the alpha subunit of hypoxia-inducible factor- α (HIF α), can coordinate tissue inflammation and tumorigenesis. We previously generated mice with conditional *Vhlh* knockout in kidney tubules, which resulted in severe inflammation and fibrosis in addition to hyperplasia and the appearance of transformed clear cells. Interestingly, the endothelial cells (EC), although not subject to genetic manipulation, nonetheless showed profound changes in gene expression that suggest a role in promoting inflammation and tumorigenesis. Oncostatin M (OSM) mediated the interaction between *VHL*-deficient renal tubule cells and the ECs, and the activated ECs in turn induced macrophage recruitment and polarization. The OSM-dependent microenvironment also promoted metastasis of exogenous tumors. Thus, OSM signaling initiates reconstitution of an inflammatory and tumorigenic microenvironment by *VHL*-deficient renal tubule cells, which plays a critical role in ccRCC initiation and progression.

Significance: A novel mechanism of cross-talk between ECs and *VHL*-deficient kidney tubules that stimulates inflammation and

tumorigenesis is discovered, suggesting OSM could be a potential target for ccRCC intervention.



Introduction

Many forms of cancer, including renal cell carcinoma (RCC), have been linked to chronic tissue inflammation (1–3). While immune cells

and myofibroblasts have been recognized as major contributors to chronic inflammation, the endothelium has not been widely regarded as an active player in the pathogenic process. Recent findings, however, indicate that vascular endothelial cells (EC) in fact play a crucial role in the inflammatory response and in tumor progression, beyond the scope of the well-known hypoxia-induced neoangiogenesis for oxygen and nutrient supply (4).

Clear-cell RCC (ccRCC) is the most prevalent histologic subtype of RCC, and is resistant to most conventional chemo- and radiation therapies. Interestingly, about 70% of the ccRCC cases are associated with genetic or epigenetic defects in the von Hippel–Lindau (*VHL*) tumor-suppressor gene (5, 6). The important role of loss of *VHL* function in tumorigenesis is associated with upregulation of hypoxia-inducible factor- α (HIF α ; refs. 5, 7). Upregulation of HIF transcription factor has been linked to neoangiogenesis, metabolic imbalance, and malignant progression. However, how loss of *VHL* function in parenchymal cells influences the surrounding microenvironment, and thus initiates the formation of ccRCC, still remains unclear.

We previously generated a conditional *Vhlh* (the mouse *VHL* allele) knockout (KO, exon 1 deleted) mouse model (*Hoxb7-Cre-GFP; Vhlh^{loxP/loxP}*) in a subpopulation of kidney tubule cells, including those in the collecting ducts, a subset of distal and proximal tubules, and ascending Henle’s loops (8). The KO kidney tissue exhibits

¹Department of Biomedical Sciences and Engineering, National Central University, Taoyuan City, Taiwan, Republic of China. ²Center for Chronic Disease Research, National Central University, Taoyuan City, Taiwan, Republic of China. ³Graduate Institute of Biomedical Sciences, China Medical University, Taichung, Taiwan, Republic of China.

Note: Supplementary data for this article are available at Cancer Research Online (<http://cancerres.aacrjournals.org/>).

Current address for T. Hsu: Graduate Institute of Biomedical Sciences, China Medical University, Taichung, Taiwan, Republic of China.

Corresponding Author: Tien Hsu, Graduate Institute of Biomedical Sciences, China Medical University, No. 91 Hsueh-Shih Road, Taichung, Taiwan 40402, ROC. Phone: 886-42205212, ext. 7716; E-mail: tienhsu@mail.cmu.edu.tw

Cancer Res 2021;81:5060–73

doi: 10.1158/0008-5472.CAN-21-0345

This open access article is distributed under Creative Commons Attribution-NonCommercial-NoDerivatives License 4.0 International (CC BY-NC-ND).

©2021 The Authors; Published by the American Association for Cancer Research

severe interstitial inflammation and fibrosis in addition to hyperplasia and appearance of transformed clear cells, but no full-blown ccRCC (8, 9). Furthermore, the inflammatory response of the *VHL*-deficient tubule cells is the result of endoplasmic reticulum (ER) stress caused by metabolic imbalance (9).

During the course of studying the etiology of tissue inflammation in the conditional *Vhlh* KO kidney, we noticed expression of proinflammatory markers such as phosphorylated c-Jun N-terminal kinase (p-Jnk) in the vascular EC, even though the ECs were not subject to genetic manipulations in the *Vhlh* KO mice. This prompted us to propose that in the *Vhlh* KO kidney, ECs are activated and/or inflamed, and that these activated ECs may play a critical role in the protumorigenic microenvironment. We report here that these ECs undergo profound changes in the gene expression program, showing characteristics of inflammatory response and mesenchymal transition, both *in vitro* and *in vivo*. Furthermore, these changes are induced by oncostatin M (OSM) emanating from the *VHL/Vhlh*-deficient cells. These dysfunctional, or activated, ECs reciprocally help establish a microenvironment that promotes tissue inflammation, tumor-cell proliferation, and metastasis.

Materials and Methods

A detailed description of cellular and biochemical experimental procedures is described in Supplementary Materials and Methods. The primers for real-time PCR are listed in Supplementary Table S1. Antibodies and staining conditions used in immunofluorescence and IHC are listed in Supplementary Table S2.

Cell culture

All cell lines used were purchased from cell-line repositories [ATCC, or Bioresource Collection and Research Center (BCRC)] that perform authentication. Standard practice in our laboratory consists of the following: Upon receiving the samples from the suppliers, the cells were grown to approximately 70% to 80% confluency, expanded, examined for the presence of mycoplasma using EZ-PCR Mycoplasma Detection Kit (from Biological Industries, SKU: 20-700-20), and collected for storage in liquid N₂ using standard protocol. Depending on the proliferative characteristics of the cell lines, the expanded cells were rinsed and divided into 15 to 30 1 ml aliquots each containing an equivalent of approximately 25% to 40% confluent cell number in a 10-mm dish. For experimentation, each frozen aliquot was used and propagated for no more than 10 passages depending on the viability of the cell lines. A portion of the regrown cells was stained with DAPI to ensure the lack of *Mycoplasma* contamination. Other experimental details are described in Supplementary Materials and Methods.

Animals

The *Hoxb7-Cre-GFP; Vhlh^{loxP/loxP}* mouse strain has been described previously (8). OSM receptor KO mouse (*Osmr^{-/-}*) was purchased from RIKEN [B6.129S-Osmr<tm1Mtan> (RBRC02711)] and has been described (10). NOD/SCID mice (*NOD.CB17-Prkd^{scid}/NcrCr1*) were purchased from BioLASCO. All experiments with mice were performed in accordance with the protocol approved by the Institutional Animal Care and Use Committee of National Central University.

Human ccRCC samples

Human paraffin-embedded tissue array of ccRCC was purchased from US Biomax Inc. (KD241). Other human ccRCC samples were collected from patients at Triservice General Hospital, Taiwan, Institutional Review Board no. 2-106-05-079.

Statistical analysis

Statistical analysis was performed using unpaired two-tailed Student *t* test (two-group comparison) or one-way ANOVA with Tukey *post hoc* test (multiple-group comparison). The difference between groups was considered statistically significant when the *P* value was < 0.05.

Data availability

mRNA transcriptome of ECs has been uploaded to the GEO (#GSE159754). All other data in this study are available from the corresponding author upon request.

Results

Conditional *Vhlh* KO mice exhibit inflammatory, clear-cell, and adenoma phenotypes

For brevity, the conditional mutant mouse (*Hoxb7-Cre-GFP; Vhlh^{loxP/loxP}*) is named *Vhlh^{KO}* and the wild-type mouse (*Hoxb7-Cre-GFP* or *Vhlh^{loxP/loxP}*) is named WT in this report. As shown in Fig. 1A, the KO kidney shows prominent phenotypes at 3 months of age, including formation of clear-cell clusters with irregular cell shape, infiltration of immune cells, increased vasculature, fibrosis, and appearance of inflammatory foci (clusters of immune cells and dilated tubules) with a penetrance of more than 90%, consistent with previous findings (8). These inflammatory foci are often associated with increased number of enlarged blood vessels (insets, Fig. 1A). Since *Hoxb7-Cre-GFP* is marked by the GFP reporter, it is possible to confirm that the tubule phenotypes are associated with *Vhlh* inactivation. As shown in Fig. 1B, wild-type kidney (*Vhlh^{loxP/loxP}*) without *Hoxb7-Cre-GFP* shows no GFP staining, while wild-type kidney carrying only *Hoxb7-Cre-GFP* shows GFP-expressing cells in both cortical and medullary tubule epithelia that are morphologically normal. In contrast, in *Vhlh^{KO}* kidney, the GFP-expressing tubules in both cortex and medulla exhibit multilayering with presence of clear cells (Fig. 1C). Accumulation of immune cells is also notable in the vicinity of abnormal tubules.

Our previous study has indicated that tissue inflammation in the *Vhlh* KO kidney is correlated with atopic activation (phosphorylation) of Jnk and NF- κ B in the *VHL*-deficient cells resulting from ER stress (9). However, we have subsequently noted that p-Jnk expression is also enriched in vasculatures near the abnormal tubules in *Vhlh^{KO}*, but not in WT (Fig. 2A), even though these ECs do not harbor genetic manipulations. Similarly, in human ccRCC samples, p-JNK is not present in the normal adjacent tissue (NAT), while strong p-JNK expression is detected in the ECs (CD31⁺) surrounding clear-cell clusters in the ccRCC proper (Fig. 2B). It is also notable that these p-JNK/p-Jnk-expressing blood vessels are dilated and disorganized in *Vhlh* KO mouse kidney and in human ccRCC.

Also, as shown in Fig. 2C, vascular density of *Vhlh^{KO}* tissue is increased by nearly 2-fold compared with WT. We then assayed *in vivo* vascular permeability by injecting FITC-conjugated dextran (500 kDa) via tail vein. As shown in Fig. 2D, IHC shows diffusion of FITC around the blood vessels in the peritubular space in *Vhlh^{KO}* mice, indicating that FITC-dextran has leaked out of the blood vessels and therefore cannot be cleared from circulation. Note that the microvasculature in glomeruli shows substantial permeability even in WT. This is consistent with the characteristics of these fenestrated vessels. These results suggest that alteration in vascular integrity already occurs before frank ccRCC is formed.

Activation of ECs in *Vhlh^{KO}* tissue

To understand the potential role of ECs in the *Vhlh^{KO}* phenotypes, we isolated ECs from WT (*Hoxb7-Cre-GFP*) and *Vhlh^{KO}* tissues and

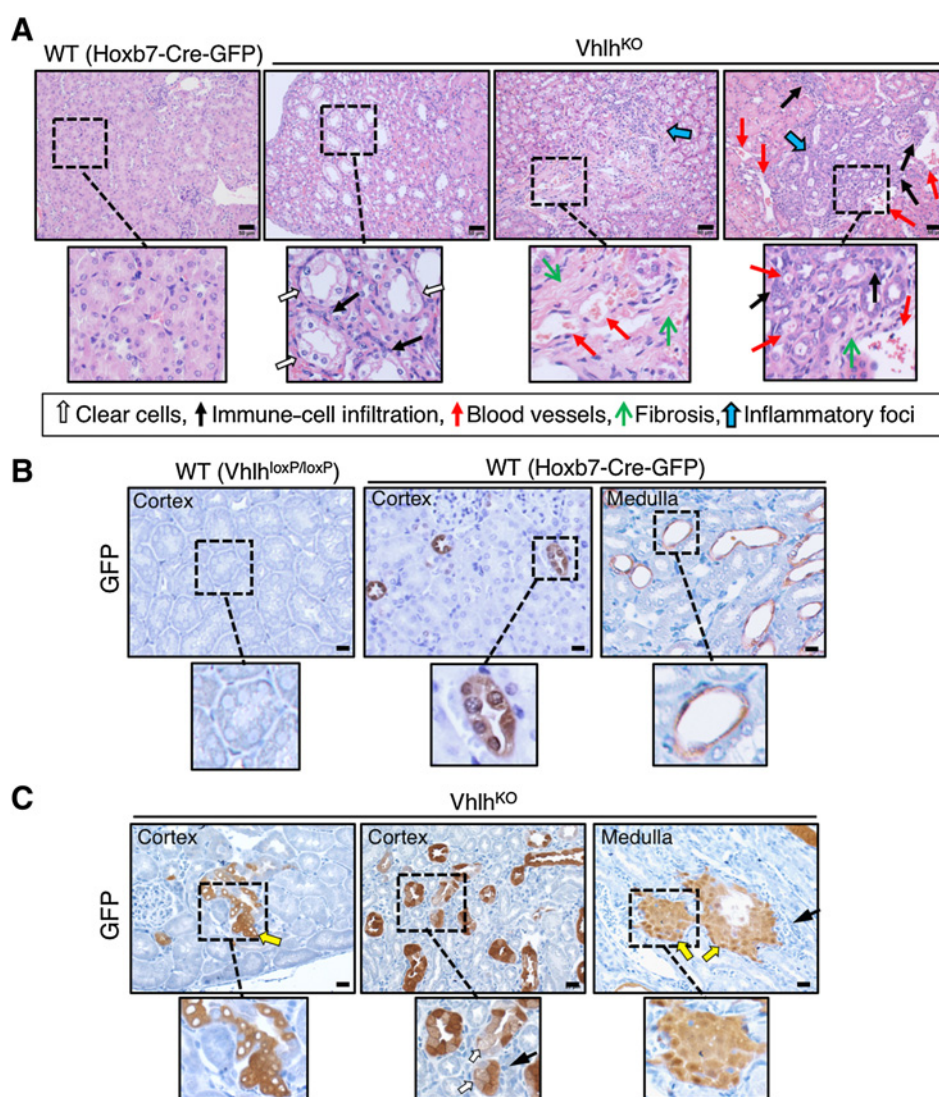


Figure 1.

Conditional *Vhlh* KO kidney shows inflammatory and tumorigenic phenotypes. Representative images of 4 to 5 animals are shown. **A**, Hematoxylin and eosin staining of kidney sections from 3-month-old mice, comparing wild-type (WT, *Hoxb7-Cre-GFP*) and mutant (*Vhlh*^{KO}, *Hoxb7-Cre-GFP*; *Vhlh*^{loxP/loxP}). White block arrows, clear cell clusters; black arrows, infiltrated immune cells; red arrows, blood vessels (containing red blood cells); sharp green arrows, fibrosis (pinkish fibrous staining); blue block arrows, inflammatory foci. Note that the inflammatory foci often contain an increased number of blood vessels. Bars, 50 μ m. **B**, GFP staining of kidney sections from 3-month-old wild-type mice of the genotype *Vhlh*^{loxP/loxP} or *Hoxb7-Cre-GFP*; *Vhlh*^{loxP/loxP} shows no GFP and *Hoxb7-Cre-GFP* shows GFP staining in morphologically normal tubules in cortex and medulla. Bars, 20 μ m. **C**, GFP staining of kidney sections from 3-month-old *Vhlh*^{KO} mice. GFP is expressed in abnormal tubules in cortex and medulla. These mutant cells show adenoma-like multilayering (yellow block arrows) and clear-cell (white block arrows) phenotypes. There is also an increase in immune-cell infiltrates near the mutant tubules (black arrows). Bars, 20 μ m.

performed transcriptome analysis using RNA sequencing (RNA-seq). The RNA-seq result has been deposited in Gene Expression Omnibus (GEO; #GSE159754).

Anti-CD31 antibody-conjugated magnetic beads were used to isolate kidney ECs. These isolated ECs show high viability (>99%), and the purity of isolated CD31⁺ cells is approximately 95% (Supplementary Fig. S1A). Although CD31 is also expressed by lymphatic ECs, the expression level is much lower in the lymphatic vessels than in the vasculature (11). We therefore used stringent conditions for purifying ECs and expected that our EC preparation would contain few contaminating lymphatic ECs. Indeed, the expression levels of lymphatic EC gene *Podoplanin* in the RNA-seq-based transcriptome are low in either WT or *Vhlh*^{KO} samples (40–60-fold lower than those of CD31; Supplementary Table S3). The transcriptome shows that the ECs from *Vhlh*^{KO} (ECs-KO) kidneys exhibit profound changes in the gene expression program, compared with the counterparts isolated from WT (ECs-WT) animals (Supplementary Fig. S1B and S1C).

Overall, there are 450 genes upregulated and 483 genes down-regulated more than 1.5-fold (Log_2) and with fragments per kilobase of

exon per million reads (FPKM) over 5 in ECs-KO compared with ECs-WT (Supplementary Fig. S1C and Supplementary Table S3). The most upregulated gene is *Arginase 1* (*Arg1*). Upregulation of *Arg1* in EC has been linked to imbalance of nitric oxide (NO) synthesis, referred to as “eNOS uncoupling,” and suggested to play an important role in EC dysfunction and activation (12). For brevity, we will describe these ECs-KO as activated in this report.

Bioprocess Enrichment analysis shows that these differentially expressed genes are mainly involved in tissue inflammation. In addition, the enriched bioprocesses in cell migration and cell-shape regulation indicate mesenchymal transition of these ECs-KO, which has been suggested to play an important role in fibrosis (13–15). The Disease and Function analysis reveals that ECs-KO exhibit increased function of EC migration, growth of connective tissue, proliferation, tumor progression, and development of vasculature, as well as decreased function of glucose metabolism and acute inflammatory (i.e., antipathogen and antitumor) response (Supplementary Fig. S1C). These gene expression patterns are therefore consistent with the fibrotic and tumorigenic phenotypes observed in the *Vhlh*^{KO} kidney.

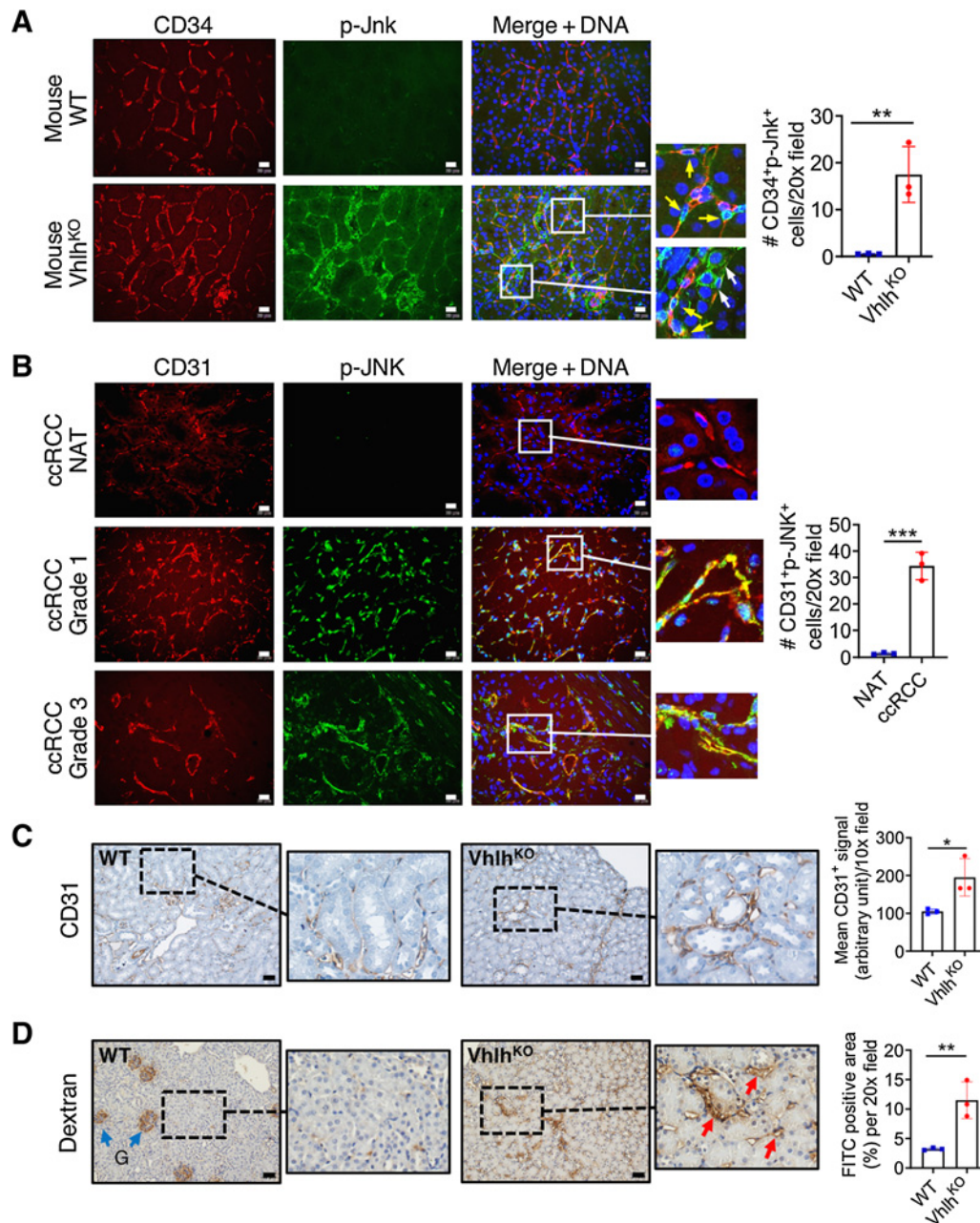


Figure 2.

ECs in Vhlh^{ko} mouse or human ccRCC kidney tissues exhibit increased p-JNK/p-Jnk expression, vasculature density, and vessel permeability. **A**, Representative images of mouse kidney sections double stained for CD34 and p-Jnk ($n = 6$). Because of the antibody host-source compatibility in double staining, CD34, instead of the more common CD31, was used for marking mouse ECs. p-Jnk is detected in abnormal tubules (white arrows) and in the adjacent ECs (CD34⁺ cells, yellow arrows) in Vhlh^{ko} compared with WT. Bars, 20 μ m. **B**, Representative images of human ccRCC tissue sections double stained for CD31 and p-Jnk ($n = 6$). p-JNK was not detected in NAT. In ccRCC tissue, p-JNK is colocalized with CD31 in both grade 1 and grade 3 tumors. Bars, 20 μ m. **C**, The number of CD31⁺ cells is increased nearly 2-fold in Vhlh^{ko} tissues compared with WT. Bars are 50 μ m. **D**, Kidney sections were stained for FITC after tail-vein injection of FITC-dextran. Diffused FITC is detected surrounding blood vessels near abnormal tubules (red arrows), while in WT tissues, FITC is detected only within the glomeruli (G). Bars, 50 μ m. Each data point in the graphs represents an individual animal or human tissue sample, and is the average number of four to five microscopic fields from each section. The data are presented as mean \pm SD, and the P values are calculated by two-tailed unpaired Student t test. *, $P < 0.05$; **, $P < 0.01$; ***, $P < 0.001$.

Among the upregulated genes, several are typically associated with chronic inflammation and fibrosis (Supplementary Fig. S2A). In the context of inflammatory response, ECs-KO show high expression of *Hepatitis A virus cellular receptor 1 (Havcr1)* and *Lipocalin 2 (Lcn2)*. *Havcr1* is a biomarker for kidney injury (16) and early detection of kidney cancer (17). *Lcn2* has been recognized as a biomarker for acute kidney injury and chronic kidney disease (18). Also, IL6 is the most upregulated cytokine in ECs-KO. IL6 is produced at the site of inflammation and plays a crucial role in inflammatory response (19). IL6 from ECs has been shown to induce alternative macrophage activation (20) and promote tumor growth (21). There are also many upregulated genes related to immune-cell infiltration, including chemokines (*Ccl2* and *Ccl7*) that recruit monocytes/macrophages, and adhesion molecules that capture circulating leukocytes, such as *E-selectin (Sele)*, *P-selectin (Selp)*, *Intercellular adhesion molecule 1 (Icam1)*, and *Vascular cell adhesion molecule 1 (Vcam1)*. Interestingly, markers associated with mesenchymal transition are enriched, including *Snail1 (Snai1)*, *Fibronectin 1 (Fn1)*, *Collagen 1 (Col1a1)*, and *Chitinase-like-3 (Chil3)*, consistent with the Bioprocess Enrichment analysis described above. Overexpression of these markers was verified by qRT-PCR (Supplementary Fig. S2B). Consistent with these gene-expression patterns, significant tissue fibrosis in the *Vhlh*^{KO} kidney has been reported previously (8, 9) and is confirmed here (Supplementary Fig. S2C). Also, ECs-KO indeed express high levels of *Snai1* (Supplementary Fig. S2D). In addition, *Icam1* is highly expressed in the vessels of *Vhlh*^{KO} kidney (Supplementary Fig. S2E), and ICAM1-positive vessels are associated with ccRCC (Supplementary Fig. S2F).

Osm is a major regulator of EC activation in conditional *Vhlh* KO mice

We suspect that the changes in EC-KO transcriptome are likely the result of paracrine action directly or indirectly emanating from the *Vhlh*-mutant tubule cells. Ingenuity Pathway Analysis (IPA) was therefore employed to identify the potential upstream regulators. Supplementary Table S4 shows top 15 potential upstream regulators with high increase values (based on z-score) that are statistically significant. Among these, OSM signaling shows the highest score. It is noteworthy that a few other candidates also belong to or are related to OSM signaling, including STAT3, IL6, and OSM receptor (OSMR).

OSM and IL6 belong to the same family of cytokines (19). They regulate overlapping but nonidentical sets of downstream genes, mainly via the JAK signal transducer and activator of transcription proteins (STAT)-signaling pathway. OSM is likely a more upstream regulator than IL6 for the following reasons: First, IL6 is known to be an OSM target gene in ECs (22, 23) and our EC transcriptome analysis also shows upregulation of IL6 in ECs-KO (Supplementary Table S3). Second, *Osm* is not a downstream target of IL6 yet the target genes of *Osm*, but not of IL6, such as *Icam1* and *Sele* are overexpressed in ECs-KO. Recently, OSM has emerged as a major mediator in tissue fibrosis (24, 25) and may play an important role in the development of certain cancers (26, 27). Taken together, we consider *Osm* the most relevant signaling pathway in the activation of ECs in *Vhlh*^{KO} tissue.

OSM and other IL6-related family of cytokines share some but not all receptor components. In human, OSM signaling is initiated by binding of OSM to its type-I receptor complex (LIFR β /gp130) or type-II receptor complex (OSMR β /gp130) whereas mouse *Osm* shows high affinity only to type-II receptor (28). We will refer to OSMR β as OSMR henceforth. ECs are the most probable target of OSM signaling because ECs express the highest level of OSMR in normal tissues (23, 29), and

the levels of *Osmr* and gp130, but not *Lifr*, are further upregulated by Osm signaling and in *Vhlh*^{KO} (Fig. 3A; ref. 30). In order to establish the interactive network in the microenvironment of *Vhlh*^{KO} kidney tissue, we first sought to identify the source of Osm. As shown in Fig. 3B, WT tissue does not express appreciable level of Osm in any cells, while in *Vhlh*^{KO} tissue, high levels of OSM are detected in morphologically abnormal *Vhlh*-mutant tubule cells (Fig. 3B, lower panels). In addition, in human ccRCC samples, OSM and carbonic anhydrase IX (CAIX, a marker for *VHL*-mutant ccRCC cells) are undetectable in the NAT, while high levels of OSM are detected in CAIX-positive ccRCC cells (Fig. 3C).

Currently there is no suitable anti-*Osmr* antibody for mouse-tissue IHC. However, an approximately 3-fold increase in *Osmr* mRNA level can be detected in primary ECs isolated from *Vhlh*^{KO} kidney compared with WT (Fig. 3A, right panel). In human ccRCC samples, high levels of OSMR protein is detected in cancer-associated vessels (CD31⁺), but not in normal adjacent tissue (NAT; Fig. 3D). We therefore conclude that OSM signaling mediates the interaction between *Vhlh*-mutant tubule cells and the ECs. Analysis of data from The Cancer Genome Atlas (TCGA) reveals that high expression levels of OSM (Supplementary Fig. S3A) and OSMR (Supplementary Fig. S3B) in ccRCC are associated with poor survival.

The characteristics of OSM-activated ECs

Two types of ECs, HUVECs or HMEC-1, were cocultured with human noncancerous kidney tubule cell line HK-2 with or without *VHL* knockdown (KD). Noncancerous kidney tubule cells were used because we were interested in the early events in the initial stage of tumorigenesis. Established malignant ccRCC cell lines accumulate many genomic alterations that are subsequent to tumor initiation and therefore could not serve this purpose. The efficiency of *VHL* KD was monitored by the reduction of *VHL* protein and increased expression of HIF1 α protein (Fig. 4A; Supplementary Fig. S4A and S4B). Importantly, *VHL* KD results in increased expression of OSM in HK-2 cells (Fig. 4A; Supplementary Fig. S4C) and in conditioned media (Fig. 4B). In order to examine the cross-talk between kidney tubule cells and ECs, we employed a coculture system using the Boyden chamber (Fig. 4C). When cocultured with *VHL* KD HK-2, as compared with wild-type HK-2, HMEC-1 exhibits increased levels of OSMR, OSM downstream signal transducer p-STAT3 (activated STAT3), and target gene products ICAM1 and SNAIL1 (Fig. 4D, compare lane 1 with lanes 2 and 3; Supplementary Fig. S5A–S5D). The increase of OSM downstream target genes (p-STAT3, SNAIL1, and ICAM1) in ECs activated by *VHL*-deficient HK-2 was reverted when OSMR was knocked down (Fig. 4D, compare lane 4 with lanes 5 and 6, and lane 7 with lanes 8 and 9; Supplementary Fig. S5A, S5C, and S5D). When neutralizing OSM antibody was added to the conditioned media, the expression of these target genes in ECs was also reduced to the background level (Fig. 4D, lanes 10–12; Supplementary Fig. S5A, S5C, and S5D).

To verify the direct effect of OSM on ECs, human recombinant OSM (rOSM) was added to the media of EC single culture. p-STAT3, ICAM1, and VCAM1 show dose-dependent increase in ECs (Supplementary Fig. S6A). In addition, qRT-PCR also confirmed the rOSM effect on the expression of some of the target genes identified in the EC transcriptome, including *CCL2*, *CCL7*, *SELE*, and *IL6* (Supplementary Fig. S6B). The uncropped protein blot and quantification in Fig. 6A are shown in Supplementary Fig. S7A–S7C. Together, these results indicate that OSM secreted by *VHL*-deficient kidney tubule cells is the major activator of the inflammatory program in the ECs.

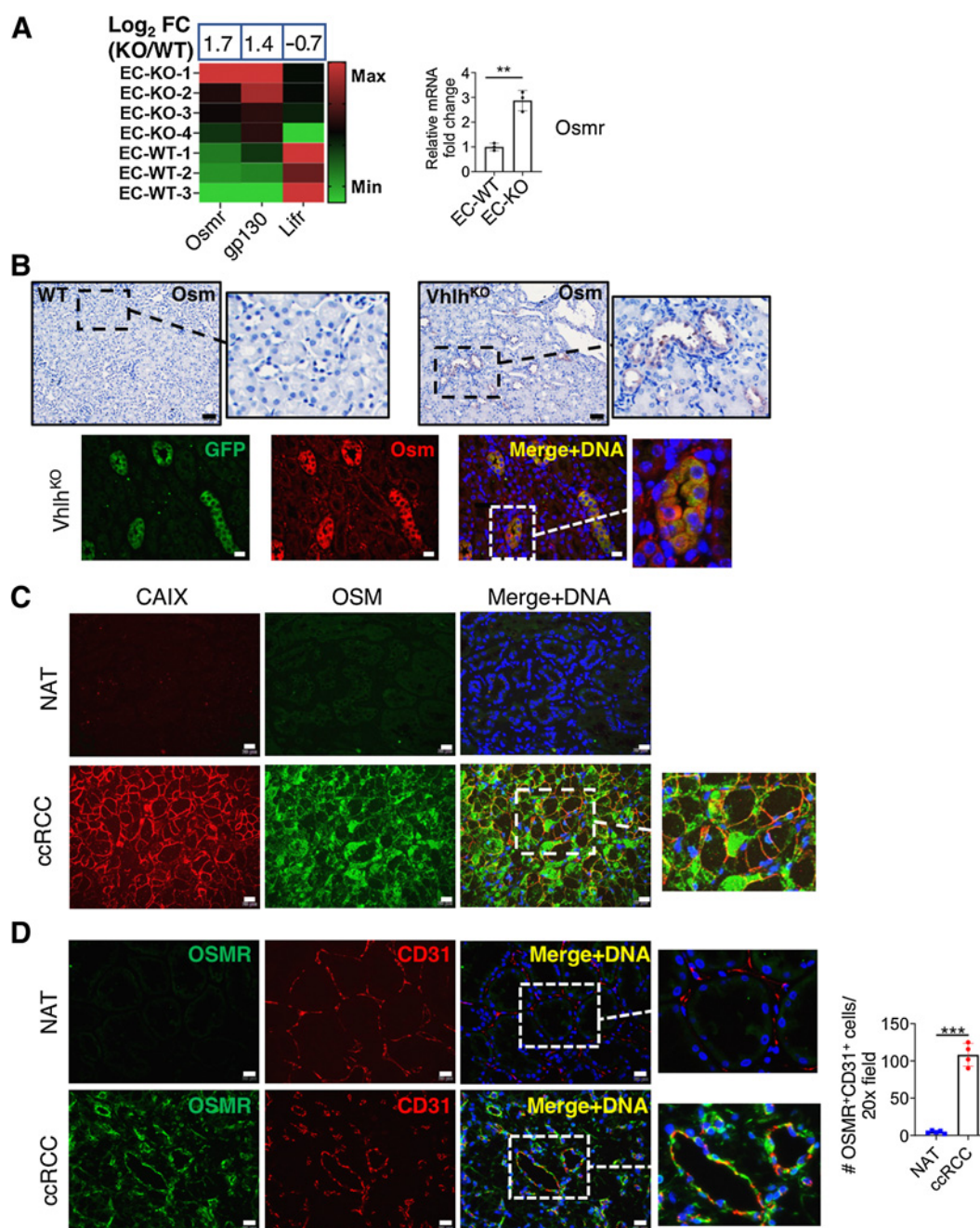


Figure 3.

Cell-type-specific expression of OSM and OSMR. **A**, Overexpression of *Osmr* components in activated ECs from *Vhlh*^{KO} kidney. Heatmap of the transcriptome data shows *Osmr* subunits, *Osmr* and *gp130*, are overexpressed, while the alternative receptor, *Lifr*, is not (left). Overexpression of *Osmr* is validated by qRT-PCR analysis of RNA purified from the primary ECs of *Vhlh*^{KO} or WT kidneys (right). **B**, Mouse kidney sections from WT and *Vhlh*^{KO} were stained for *Osm*, which is overexpressed in the abnormal kidney tubules from *Vhlh*^{KO} (top right; *n* = 4) but not in WT (top left; *n* = 4). Double staining for GFP (*Vhlh* KO cell reporter) and *Osm* shows enriched expression of *Osm* in *Vhlh* KO cells (bottom; *n* = 4). Bars, 50 μ m in top panels and 20 μ m in bottom panels. **C**, Double staining of OSM and CAIX (a HIF target and marker of *VHL*-mutant ccRCC cells) in human ccRCC samples (*n* = 6). OSM and CAIX are undetectable in NAT. In contrast, OSM is strongly expressed in CAIX⁺ cells in cancer tissue. Bars, 20 μ m. **D**, Human ccRCC samples double stained for CD31 and OSMR (*n* = 6). OSMR is not expressed in NAT but overexpressed in the CD31⁺ ECs around the clear-cell clusters in cancer tissue. Bars, 20 μ m. Each data point in the graphs represents an individual animal or patient sample, and is the average number of four microscopic fields from each section. The data are presented as mean \pm SD, and the *P* values are calculated by two-tailed unpaired Student *t* test. **, *P* < 0.01; ***, *P* < 0.001.

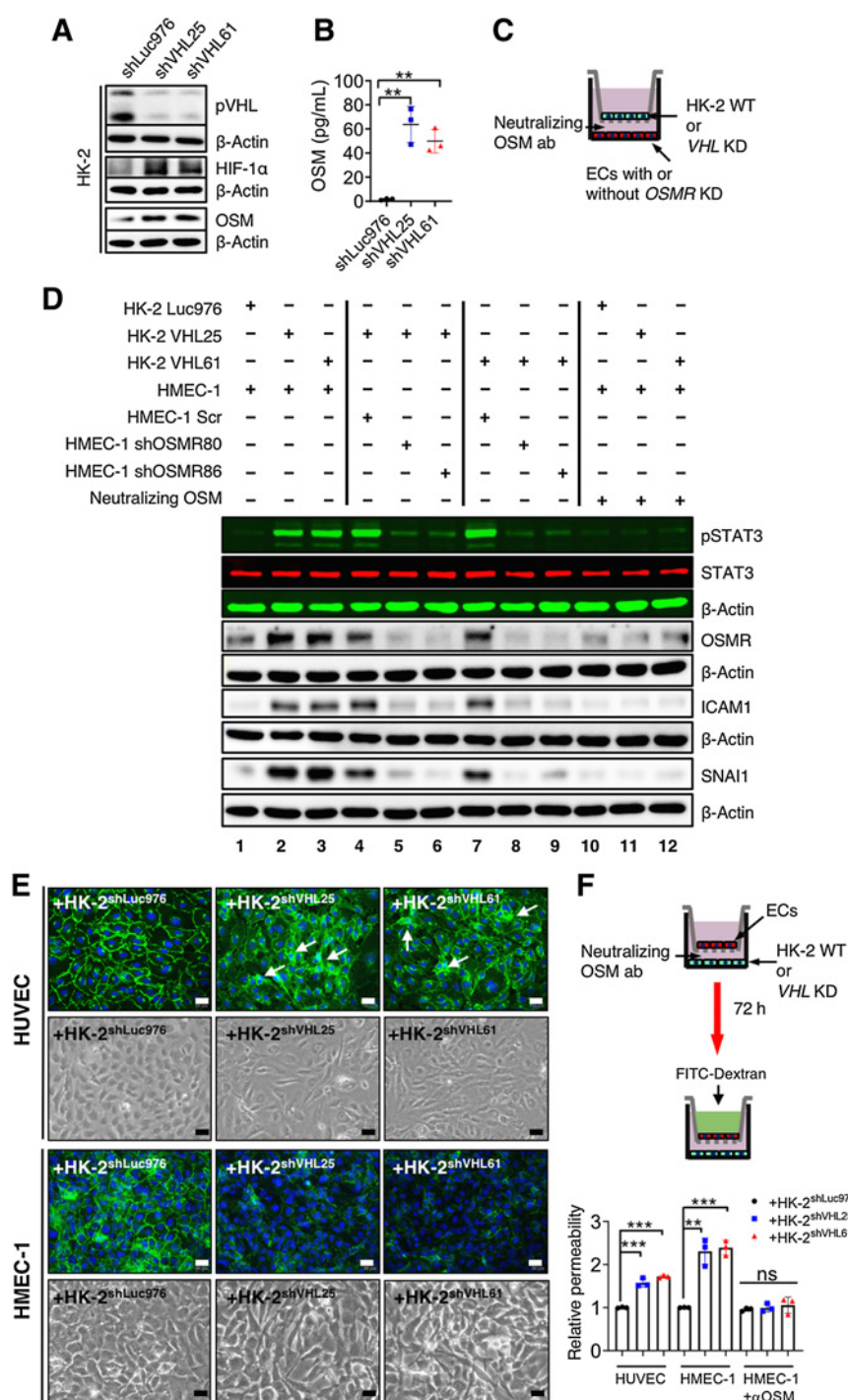


Figure 4. OSM signaling mediates interaction between human kidney tubule cells and ECs. **A**, HK-2 cells were transfected with lentiviral vectors expressing control shRNA (shLuc976) or one of the two *VHL*-specific shRNAs (shVHL25 and shVHL61). Western blot analysis of protein extracts from the three cell lines shows decreased expression of pVHL and increased expression of OSM and HIF1α. Uncropped Western blots and quantification are shown in Supplementary Fig. S4. **B**, Conditioned media from the above three cell lines were measured by ELISA for the presence of OSM. *VHL* KD results in significant increase in the secretion of OSM. shRNA, short hairpin RNA. **C**, Schematics of the Boyden chamber coculture system. **D**, HK-2 cells with or without *VHL* KD were cocultured with HMEC-1 with or without *OSMR* KD, or in the presence or absence of neutralizing anti-OSM antibody in the coculture media. The expression levels of OSM downstream signaling markers were analyzed by Western blot. Uncropped Western blots and quantification are shown in Supplementary Fig. S5. **E**, Morphology and VE-cadherin relocation of EC (HUVEC and HMEC-1) monolayer cocultured with wild-type HK-2 (shLuc976) or *VHL* KD HK-2. White arrows point to cytoplasmic relocation of VE-cadherin in HUVEC, while in HMEC-1, the overall VE-cadherin expression is reduced. Representative images of a total of three independent experiments are shown. Bars, 20 μm. **F**, Permeability of EC monolayer cocultured with wild-type HK-2 or *VHL* KD HK-2 or in the presence of neutralizing OSM antibody (αOSM). The data are presented as mean ± SD of three independent experimental replicates, and the *P* values are calculated by two-tailed unpaired Student *t* test. ns, no significance; **, *P* < 0.01; ***, *P* < 0.001.

Endothelial-to-mesenchymal transition signature of OSM-activated ECs

Endothelial-to-mesenchymal transition (EndoMT) has been demonstrated in various fibrotic conditions (13–15) and cancer progression (31). However, we have not been able to detect cells with dual endothelial–mesenchymal markers outside of the endothelium. While this may be because ECs outside of the endothelium rapidly lose the EC-specific markers such as CD31 and VE-cadherin, in our view,

expression of EndoMT markers in ECs does not necessarily indicate transformation of the ECs into myofibroblast-like mesenchymal cells, but can result in reduced integrity of endothelial structure. Such activated state may be needed for vessel remodeling, allowing for immune-cell recruitment, extravasation, and wound healing or fibrosis (4).

To test this notion, we examined EC characteristics in the coculture system. When cocultured with wild-type HK-2, ECs

remain a typical cobblestone-like monolayer morphology. In contrast, when cocultured with *VHL* KD HK-2, ECs become spindle-shaped (Fig. 4E), with accompanying overexpression of SNAIL1 (Fig. 4D). We also found loss of cell-junction integrity revealed by diffused VE-cadherin localization (Fig. 4E). FITC-conjugated dextran was added over the EC monolayer cocultured with wildtype HK-2 or *VHL* KD HK-2 cells (Fig. 4F). Coculturing with *VHL* KD HK-2 results in approximately 2-fold increase in FITC-dextran leakage to the lower chamber (Fig. 4F). The leakiness of EC monolayer was rescued by neutralizing OSM in the coculture system (Fig. 4F). When the endothelium was directly treated with increasing dosages of rOSM, the ECs expressed increasing amounts of mesenchymal markers SNAIL1 and SLUG proteins (Supplementary Fig. S8A). These gene-expression patterns are consistent with the change of EC monolayer morphology (Supplementary Fig. S8B) and VE-cadherin localization (Supplementary Fig. S8C). rOSM treatment also resulted in an approximately 2-fold increase in leakiness of the EC monolayer (Supplementary Fig. S8D). Finally, rOSM treatment resulted in an approximately 4-fold increase in the number of ccRCC cells 786-O invading through the endothelium (Supplementary Fig. S8E). The uncropped protein blot and quantification in Supplementary Fig. S8A are shown in Supplementary Fig. S9A–S9C.

Therefore, the OSM-activated ECs display cellular and molecular changes that are likely important for the protumorigenic role of these ECs in the microenvironment.

OSM-activated ECs induce macrophage polarization toward the M2 phenotype

The conditioned media from ECs with or without rOSM pretreatment were used to stimulate macrophages derived from THP-1 (partially differentiated to CD68⁺ M0 macrophages; Supplementary Fig. S10A). We also verified that OSM was not present in the conditioned media of activated ECs; therefore OSM had no direct activating functions on the monocytes/macrophages (Supplementary Fig. S10B and S10C). The populations of all macrophages, and classically activated (M1) and alternatively activated (M2) macrophages were detected by flow cytometry using CD68, CD86, and CD163 markers, respectively. Interestingly, conditioned media from activated ECs have no effect on the total number of CD68⁺ macrophages but significantly induce the population of CD163⁺ M2 (~20–40-fold) compared with control (Supplementary Fig. S10D and S10E). The effect is specifically on M2 polarization because the M1 (CD86⁺) population is not increased.

Among the upregulated genes in the ECs-KO, IL6 is the most abundant cytokine (Supplementary Table S3), which is known to promote alternative activation of macrophages (32). Indeed, when anti-IL6 neutralizing antibody was added to the conditioned media of rOSM-activated ECs, the proportion of CD163⁺ macrophages was reduced to the control level (Supplementary Fig. S10D and S10E).

To directly compare the impact of IL6 and OSM on THP-1-derived macrophages, we treated these cells with recombinant IL6 (rIL6) or rOSM. As shown in Supplementary Fig. S11A, rOSM does not induce polarization of THP-1-derived macrophages. In contrast, rIL6 promotes THP-1-derived macrophages polarization toward the M2 type (CD163⁺) in a dosage-dependent manner (Supplementary Fig. S11B). Taken together, these results support the notion that OSM secreted by the epithelial cells does not activate the monocytic population directly but instead signals indirectly through activation of ECs.

The above analyses reveal a network of interacting cells in the tumorigenic microenvironment containing *VHL*-deficient tubule cells—i.e., *VHL*-deficient tubule cells activate ECs via OSM signaling, and ECs in turn produce at least IL6 to activate immune cells such as macrophages.

Osm signaling is important for the *Vhlh*-mutant phenotypes *in vivo*

To test the function of OSM signaling *in vivo*, we generated *Vhlh*-*Osmr* double mutant. A systemic KO strain of *Osmr* was used for the following reason: first, tissue-specific double KO requires a combination of at least 4 transgenic markers, which are cumbersome to maintain and the mice carrying double *Cre* transgenes are often unhealthy; second, *Osmr* homozygous mutant is viable and fertile with no overt developmental and health problems (10); and third, our results indicate that *Osmr* is expressed at a negligible level in the WT kidney but at a high level preferentially in the EC compartment in *Vhlh*^{KO} kidney.

The efficacy of *Osmr* KO was monitored by examining the *Osmr* protein levels in the kidney extracts from mice of the four different genotypes: *Hoxb7-Cre-GFP* (WT), *Osmr*^{-/-} (*Osmr*^{-/-}), *Hoxb7-Cre-GFP*; *Vhlh*^{loxP/loxP} (*Vhlh*^{KO}), and *Hoxb7-Cre-GFP*; *Vhlh*^{loxP/loxP}; *Osmr*^{-/-} [double KO (DBKO)]. The *Osmr* protein expression is eliminated in *Osmr* KO and in DBKO (Fig. 5A, top panel). There are no significant changes in the body weight and mobility of all 4 genotypes at 3 months of age (Fig. 5A, bottom panel), indicating that loss of *Osmr* function does not affect the general health of the animals. Also, *Vhlh* KO dramatically increased the levels of *Osmr*, GP130, and IL6 α as compared with WT (Fig. 5A; Supplementary Fig. S12A–S12C). In DBKO tissue, the increased expression of GP130 and IL6 α as a result of *Vhlh* KO is reduced to the WT level, while Lifr remains unchanged (Fig. 5A; Supplementary Fig. S12A–S12D). These results suggest the involvement of *Osmr* type II but not type I receptor in *Vhlh*^{KO} tissue.

Importantly, EC activation markers in the *Vhlh*^{KO} animals, including EC expression of p-Jnk (see Fig. 2A) and serum level of secreted selectin E (sSele), are ameliorated when *Osmr* is inactivated in DBKO (Fig. 5B and C). In addition, the expression of p-STAT3 (Y705), which is downstream of activated JAKs, is strongly expressed in ECs in *Vhlh*^{KO} but not in WT or *Osmr*^{-/-} tissue (Supplementary Fig. S13A). Similarly, in human ccRCC tissue strong expression of p-STAT3 is found in ECs of ccRCC tissue (both grade 1 and grade 3) but not in NAT (Supplementary Fig. S13B). Interestingly, expression of p-STAT3 is also seen in some tubule cells (white arrows, Supplementary Fig. S13A) and in ECs (yellow arrows, Supplementary Fig. S13A) in *Vhlh*^{KO} tissue; but in DBKO, p-STAT3 is lost in ECs but remains in some tubule cells. This is consistent with the notion that activation of ECs in *Vhlh*^{KO} is largely mediated via *Osm* signaling, while in the mutant epithelial cells, the inflammatory response is autonomously regulated via the intrinsic ER stress-induced unfolded protein response (9).

The extent of macrophage infiltration was monitored by counting the number of F4/80⁺ cells using flow cytometry, which is reduced in DBKO compared with that in *Vhlh* single KO (Fig. 5D; Supplementary Fig. S14). The fibrotic phenotype associated with *Vhlh*^{KO} is also rescued in DBKO (Fig. 5E).

The level of *Osm* in sera is below the detection limits of the ELISA assay in WT and *Osmr*^{-/-} mice, while it is significantly higher in *Vhlh*^{KO} and DBKO mice (Fig. 5F). This indicates that the serum level of *Osm* may serve as a diagnostic marker for ccRCC development.

In another course of the experiment, we used tofacitinib to block JAK-STAT signaling in *Vhlh*^{KO} tissue to test the possibility of

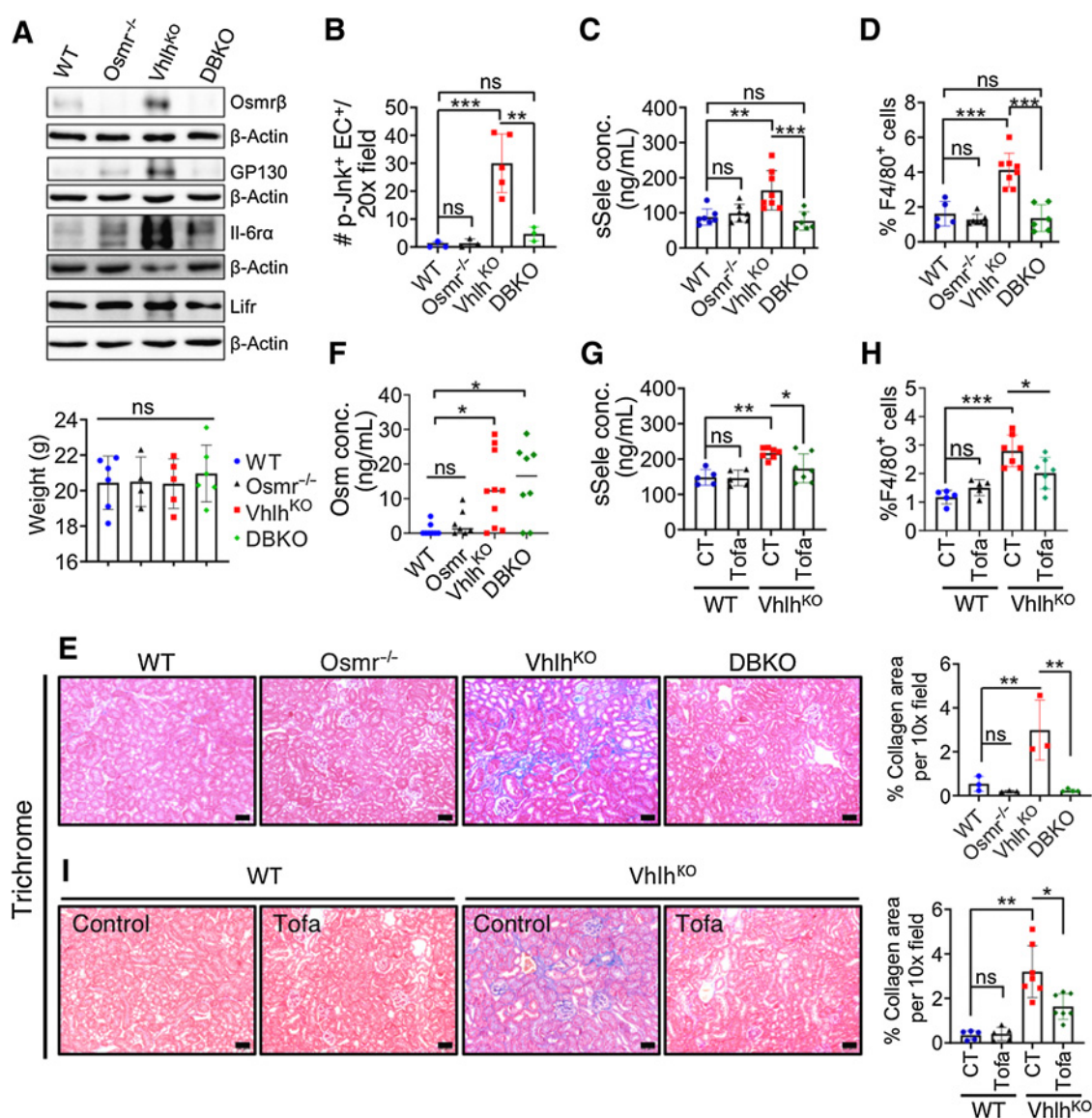


Figure 5.

Osmr inactivation rescues the *Vhlh* KO phenotypes *in vivo*. **A**, Four mouse strains of WT, *Osmr*^{-/-}, *Vhlh*^{KO}, and *Vhlh*^{KO}-*Osmr*^{-/-} DBKO were compared for their body weights at 3 months of age (bottom). The expression of OSMR components (*Osmr*β, GP130, IL6ra, and *Lifr*) in whole kidney extracts was monitored for validating the *Osmr* KO and potential feedback regulation (top). Uncropped blots are shown in Supplementary Fig. S12. **B**, The expression of p-Jnk in ECs of the four mouse strains shows an increase in *Vhlh*^{KO} and a rescue effect in DBKO. **C**, The sera of the four mouse strains show the amount of sSele is increased in *Vhlh*^{KO} compared with WT, *Osmr*^{-/-}, and DBKO. **D**, The numbers of macrophages (F4/80⁺) in the kidneys of the four mouse strains measured using flow cytometry (Supplementary Fig. S14) show increased infiltration in *Vhlh*^{KO} compared with WT, *Osmr*^{-/-}, and DBKO. **E**, Kidney sections of the four strains of mice were stained with the trichrome reagents. The amount of collagen fiber deposit (purple stain) was quantified by color metrics measurement using the ImageJ software (right panel). Each data point represents the average number per 10× view of one section from one animal. Bars, 50 μm. **F**, The concentration of Osm in sera of the four strains of mice. **G-I**, Quantification of the concentration of sSele in sera (**G**), the numbers of macrophages (**H**), and the amount of collagen fiber deposit (**I**) under pharmacologic treatment (tofacitinib, Tofa). Bars, 50 μm. The data are presented as mean ± SD, and the *P* values are calculated by one-way ANOVA (Tukey *post hoc* test). ns, no significance; *, *P* < 0.05; **, *P* < 0.01; ***, *P* < 0.001.

pharmacologic treatment. As expected, tofacitinib can markedly alleviate observed phenotypes in *Vhlh*^{KO} tissue by reducing concentration of sSele in serum (Fig. 5G), the number of F4/80-positive cells (Fig. 5H), and fibrosis (Fig. 5I).

The vessels in *Vhlh*^{KO} kidney show dramatic swollen and disorganized morphology in areas both juxtaposing and away from the mutant tubules (Fig. 6A), consistent with the activated EC phenotypes

in inflammatory or tumor tissues. This phenotype is rescued in the DBKO (Fig. 6A).

The levels of neoangiogenesis and neovascularization were examined by measuring the total number of CD31⁺ cells in the kidney suspension (Fig. 6B; Supplementary Fig. S15). The result shows that *Vhlh*^{KO} can increase the number of CD31⁺ ECs and introduction of *Osmr* KO ameliorates this phenotype. We also found that the

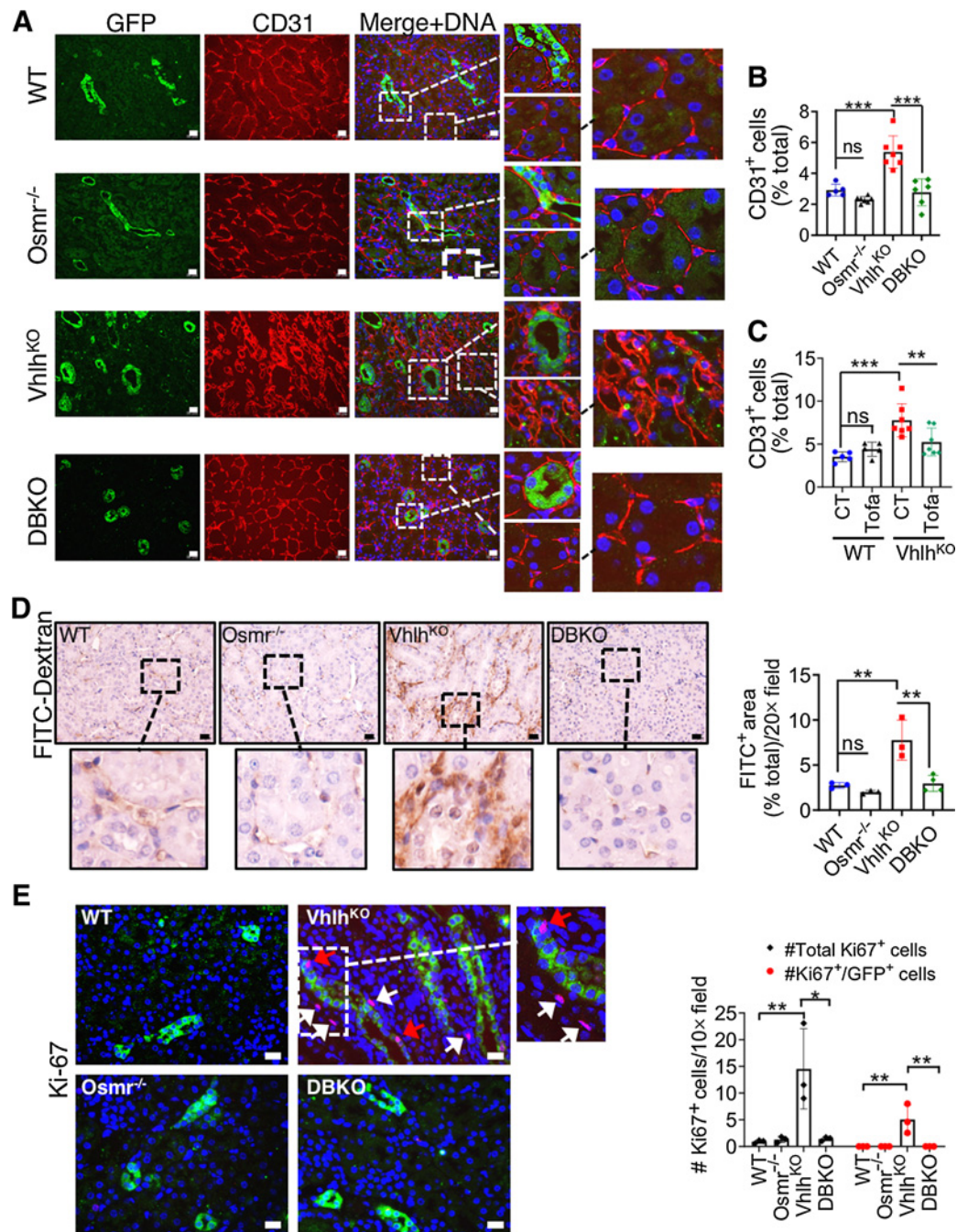


Figure 6.

Kidney vascular phenotypes and proliferation index in *Vhlh*^{KO} are rescued by *Osmr* inactivation. **A**, Kidney sections of the four indicated mouse strains were double stained for *Vhlh*-mutant cells (GFP) and CD31. The vasculature shows dramatic morphologic changes with disorganized and swollen vessels in *Vhlh*^{KO} tissue as compared with others. This phenotype is rescued in DBKO. Bars, 20 μ m. **B** and **C**, The percentages of CD31⁺ cells in whole kidney suspensions from the four genotypes (**B**) or from WT and *Vhlh*^{KO} pretreated or untreated with tofacitinib (Tofa; **C**) were quantified by flow cytometry. Each data point represents one animal. **D**, The four strains of mice as indicated were injected with FITC-dextran via tail vein. Significantly elevated diffused FITC signal is shown in *Vhlh*^{KO} tissue, which is not observed in all other genotypes. Right panel shows the quantification by colorimetric measurement using the ImageJ software. Bars, 20 μ m. Each data point represents average of four 10 \times fields of view in one section from one animal. **E**, Kidney sections from the four mouse strains were double stained for *Vhlh*-mutant cells (GFP) and Ki-67. Red arrows point to Ki-67⁺ cells that are *Vhlh* mutant. White arrows point to Ki-67⁺ cells that are not. Right panel shows the quantification by counting total Ki-67⁺ cells and Ki-67⁺GFP⁺ cells per 10 \times field of view. Bars, 20 μ m. Each data point is the average of four 10 \times fields of view in one section from one animal. The data are presented as mean \pm SD, and the *P* values are calculated by one-way ANOVA (Tukey *post hoc* test). ns, no significance; *, *P* < 0.05; **, *P* < 0.01; ***, *P* < 0.001.

angiogenic phenotypic of EC in *Vhlh*^{KO} tissue could be significantly reduced by tofacitinib (Fig. 6C).

The vascular permeability was then examined by measuring the amount of FITC-dextran in the kidney tissue after tail-vein injection. In *Vhlh*^{KO} kidney, there is a significant level of FITC signals leaking into the kidney tissue (Fig. 6D). The extent of FITC-dextran leakage is reduced to the normal level in DBKO (Fig. 6D). In addition, the number of Ki67-positive cells in both the *Vhlh*-mutant cell population (GFP⁺) and in the rest of the kidney is increased in *Vhlh*^{KO}, consistent with a hyperplastic phenotype described previously (8). This hyperplastic phenotype is completely rescued by *Osmr* KO (Fig. 6E). Note that the Ki-67-positive cells outside of the *Vhlh*-mutant tubules include both interstitial cells (probably proliferating immune cells and ECs) and those in normal tubules. This indicates that hyperplasia may be induced in genetically normal tubule cells by paracrine mitogenic factors secreted by other cell types in the microenvironment downstream of Osm signaling.

Microenvironment reconstituted by the *Vhlh*-mutant tubule cells promotes metastasis

Finally we tested whether the changes induced by OSM had any pathologic significance related to cancer progression. We used xenograft of an exogenous but syngeneic mouse melanoma cancer cell line B16 for this purpose (Fig. 7A). Human ccRCC cells cannot be used in this immune competent mouse model, and the existing mouse RCC cell line such as Renca is of a different genetic background (BALB/c) and does not grow in our *Vhlh* KO mice of the C57BL/6 background. In addition, the use of nonrenal cancer cells allowed us to test whether the OSM-activated ECs could have a general effect on tumor progression, not limited to autochthonous kidney cancer. The tumor cells were injected under the renal capsule using a Hamilton syringe as described in Supplementary Material and Methods, and we ensured that the single-cell suspension (compare Supplementary Fig. S16A with S16B) and viability (Supplementary Fig. S16C) of the injected cells were not affected. Subsequent nephrectomy examination also did not indicate leakage of the injected cells locally into normal tissues (see below). The tumor was harvested at day 14, and lung tissue was fixed and stained for GFP (marker gene transfected into B16) to quantify metastatic foci and area. Tumor growth was monitored by IVIS at day 7 and day 14 after implantation, and the actual tumor size was quantified by weight at day 14. As shown in Fig. 7B, B16 cells grow readily in the kidney of our mouse models and there is no difference in the growth rate of primary tumor, which may be because the high proliferative rate of these malignant cells cannot be further increased by the microenvironment. However, metastasis to lung is greatly enhanced in *Vhlh*^{KO} animals, and is reduced to the WT level in DBKO (Fig. 7C and D). Local invasiveness of the injected B16 tumor cells is greatly increased in *Vhlh*^{-/-} background, to the extent that no clear boundary between tumor and normal tissue can be drawn. The invasiveness is reverted to normal in DBKO (Fig. 7E). We therefore conclude that the microenvironment reconstituted by *Vhlh*-mutant cells can not only facilitate tumor initiation, but also promote metastasis of malignant cells, and that this property is dependent on OSM signaling. The metastasis-promoting activity of the *Vhlh*^{-/-} microenvironment correlates with the intratumoral vascular density (Fig. 7E).

The role of OSM signaling in promoting metastasis was further tested using a xenograft model of human ccRCC cell 786-O. Implantation of 786-O into kidney tissue of immune-

compromised NOD/SCID mice (NOD.CB17-*Prkdc*^{scid}/*NcrCr1*) was conducted (Fig. 8A). In this malignant tumor xenograft model, anti-OSM antibody treatment (Fig. 8A) does not affect primary tumor growth (Fig. 8B–D) but can inhibit metastasis (Fig. 8C and E), thus in agreement with the result with the B16 model described above.

Discussion

The influence of the inflammatory components on progression of ccRCC has been noted (1, 2). Our mouse model of *Vhlh* conditional KO in a subset of kidney tubule cells also exhibits highly penetrant inflammatory phenotypes, adenoma, and hyperplasia (Fig. 1). During analysis of the inflammatory phenotypes in the *Vhlh*^{KO} mice, we noted expression of inflammatory marker p-Jnk in the endothelial compartment of the KO kidney tissue, although these ECs were not genetically manipulated, indicating that these ECs are activated by secreted factors emanating from the *Vhlh*-mutant cells. In this report, we analyzed the transcriptome of primary ECs from the *Vhlh*^{KO} mouse kidney. Our results show that the gene expression program in ECs, a quiescent component in normal tissues, is profoundly altered in kidney tissue containing *Vhlh* deletion in the tubule cells (Supplementary Fig. S1 and S2). The gene expression program in ECs-KO is consistent with the observed tissue fibrosis and vascular abnormalities in *Vhlh*^{KO} kidney (Figs. 1 and 2).

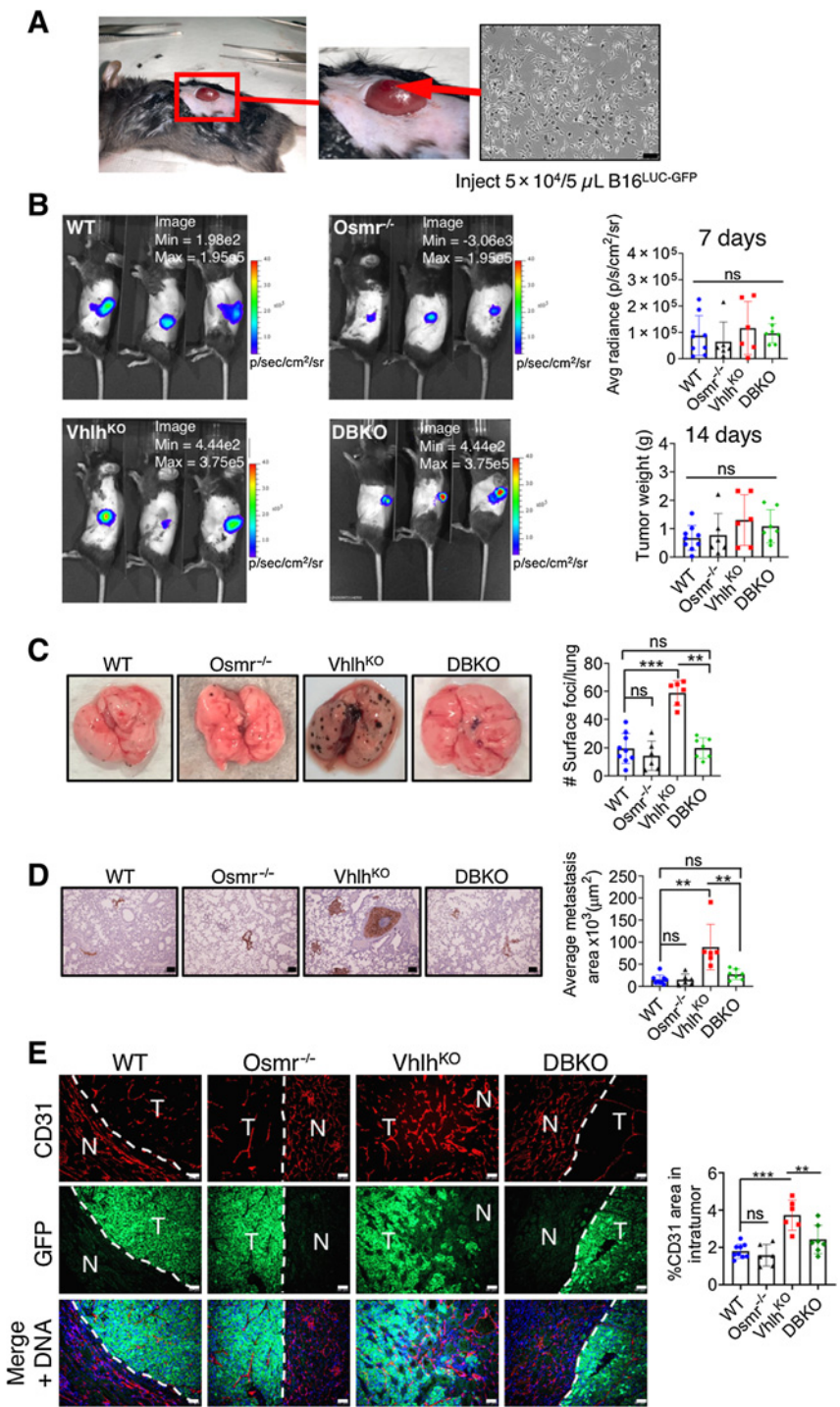
Activated ECs in *Vhlh*^{KO} mice overexpress *Sele*, *Selp*, *Vcam1*, and *Icam1*. *Sele* and *Selp* are critical molecules for capturing leukocytes, and *Vcam1* and *Icam1* are important for arresting and promoting crawling of captured leukocytes before extravasation into target tissue. Also, there is increased expression of the chemoattractants *Ccl2* and *Ccl7* in ECs-KO, indicating that *Vhlh*-mutant epithelial cells induce the activation in ECs and activated ECs, in turn, recruit circulating immune cells. This finding also explains the increased infiltration of immune cells surrounding the *Vhlh*-mutant tubules (Fig. 1).

The transcriptome results show that activation of ECs in kidney tissues is mediated mainly through the OSM pathway. OSM is overexpressed and secreted by the *VHL*-deficient kidney tubule cells and the receptor *OSMR* is expressed and induced by OSM in the ECs thus establishing an intercellular feed-forward signaling mechanism (Figs. 3, 4D, and 5A). Significantly, deletion of *Osmr* in *Vhlh*^{KO} could rescue all the inflammatory and hyperplastic phenotypes, including immune-cell infiltration, tissue fibrosis, neoangiogenesis, vascular permeability, and proliferation index (Figs. 5 and 6). It is interesting to note that *Osmr* KO in *Vhlh*^{KO} mice could normalize the vascular density of *Vhlh*^{KO} kidney to the basal level (Fig. 6). This is somewhat unexpected since the neoangiogenic phenotype in *VHL/Vhlh*-mutant tissues is normally attributed to the *VHL*-*HIF*-*VEGF* signaling axis. It is possible that the *VEGF* action may require priming by OSM signaling; e.g., in activating migratory and/or EndoMT capacity. Whether OSM plays a dominant role in neoangiogenesis in ccRCC, at least at the very early stage, requires further studies.

On the other hand, OSM has been shown to induce EndoMT and contribute to fibrosis (33). Our data demonstrate that OSM induces expression of mesenchymal transition markers such as *SNAIL1* and *SLUG* in ECs and alters the membrane localization of *VE-cadherin* (Fig. 4; Supplementary Fig. S8). Attenuating the OSM pathway diminishes fibrosis in the *Vhlh*^{KO} tissue (Fig. 5). It is therefore likely that in our system, the expression of EndoMT markers promotes loosening of the barrier function of blood vessels while inducing overproduction of matrix proteins such as collagen 1 and fibronectin *in situ* (Fig. 1; Supplementary Fig. S2A and S2B).

Figure 7.

Vhlh^{KO}-reconstituted kidney microenvironment promotes metastasis. **A**, Mouse B16 melanoma cells (marked with GFP and luciferase) were injected under the renal capsule of the four strains of mice. Bar, 100 μ m. **B**, Luciferase-carrying tumors were imaged by IVIS at 7 days after implantation. Left, representative images. Right panels show no difference in the luciferase activities (7 days) and in weights of the resected primary tumors (14 days) from the four strains of mice. Each data point represents one animal. **C**, Images of lungs from the tumor-carrying mice. Metastasized B16 foci (black spots) can be clearly seen. The number of foci on the surface is significantly higher in Vhlh^{KO} mice and can be brought down to the WT level by *Osmr* inactivation. **D**, Lung sections from the four mouse strains stained for GFP (marking the metastatic B16 cells). Bars, 100 μ m. The average area of metastasized cancer per section is significantly higher in Vhlh^{KO} than in other strains. Each data point represents one section from one animal. **E**, Local invasiveness and intratumoral vascular density of the injected B16 tumor cells in different host genetic backgrounds. White dash lines mark the boundaries of tumors (T) and normal host tissues (N). Right, quantification of intratumoral ECs (CD31⁺). Each data point represents one section from one animal. The data are presented as mean \pm SD, and the *P* values are calculated by one-way ANOVA (Tukey *post hoc* test). ns, no significance; **, *P* < 0.01; ***, *P* < 0.001.



Furthermore, recruitment and alternative activation of macrophage promoted by OSM signaling is in large part mediated via IL6 produced by activated ECs (Supplementary Fig. S10D and S10E). As such, our findings describe a network of reciprocal, cross-talking constituent cells in the tumor microenvironment that is important for ccRCC formation.

Most importantly, the microenvironment generated by the Vhlh-mutant cells can promote metastasis of an exogenous cancer cell line in Vhlh^{KO} host, and this property is dependent on the

function of OSM signaling (Fig. 7). The Osm-dependent metastasis potential of a human ccRCC line is also demonstrated in immune-deficient host (Fig. 8). There have so far been only a few reports describing the cancer-promoting function of OSM signaling (27, 34), and those few reports mostly describe the autocrine action of OSM secreted by the cancer cells *in vitro*. Our report here is a rare example that takes into account the tissue context of OSM and OSMR expression *in vivo*, and describes the important mechanism

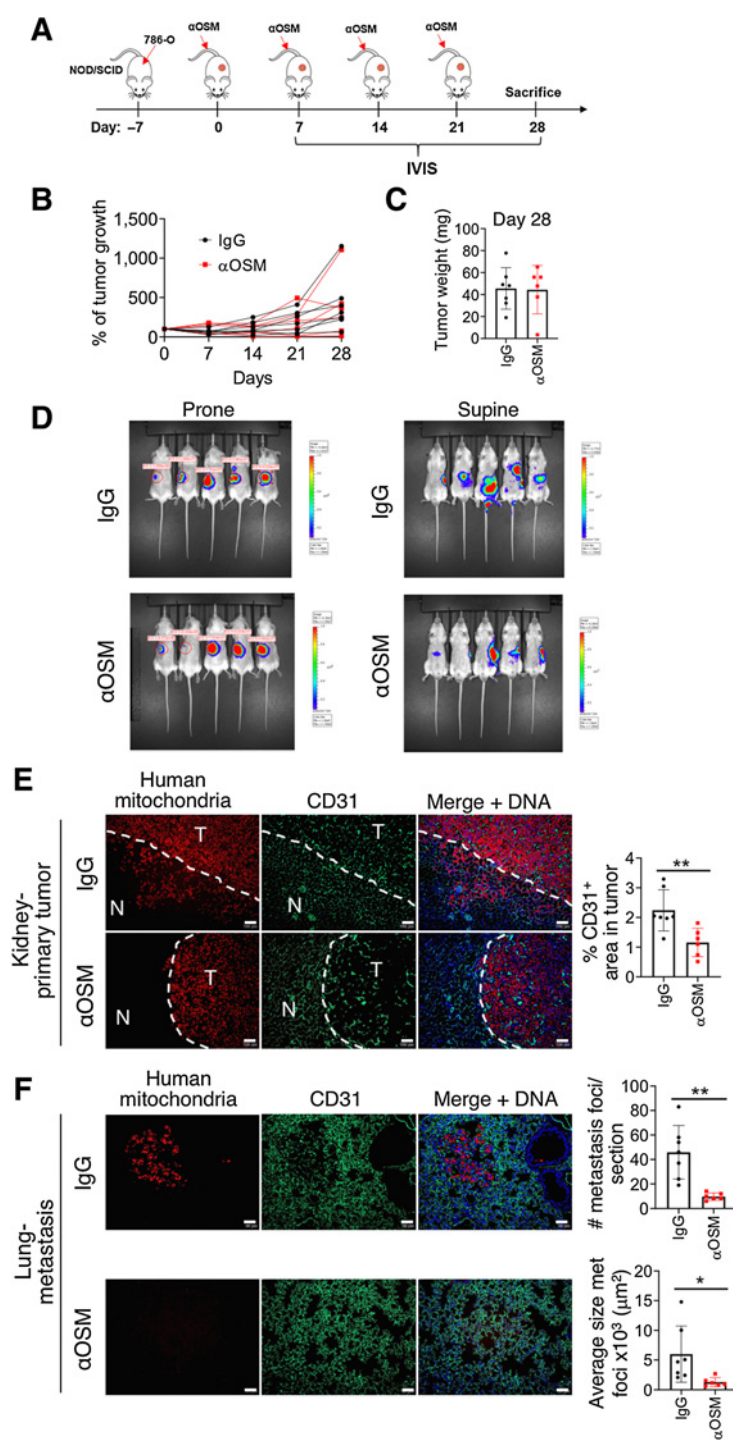


Figure 8. Metastasis of human ccRCC cells is inhibited by blocking Osm *in vivo*. **A**, Schematic illustrating the experimental design. **B**, Percentage growth of primary tumor in animal injected (α OSM) or uninjected (IgG) with antihuman OSM antibody over time. Day 0 is set at 100%. There is no difference in primary tumor growth with or without blocking OSM. **C**, Tumor weights at day 28 comparing animals treated or untreated with α OSM. **D**, IVIS imaging at day 28 in prone position (left) and supine position (right) of treated and untreated with α OSM. **E**, The invasiveness of tumor cells and intratumor vascular density in primary tumor of treated and untreated with α OSM. Tumor cells (786-O^{LUC}) were detected with human mitochondria (red), and ECs (CD31⁺) are in green. White dash lines mark the boundaries of tumor (T) and normal host tissues (N). Right, quantification of intratumoral vascular density (CD31⁺). Bars, 100 μ m. **F**, The metastasis of 786-O^{LUC} treated or untreated with α OSM in lung tissue similarly stained as in **E**. Bars, 50 μ m. Intratumoral vascular density, number of metastasis foci, and average metastasis foci area were quantified by ImageJ. Each data point represents one animal. The data are presented as mean \pm SD, and the *P* values are calculated by two-tailed unpaired Student *t* test. *, *P* < 0.05 **, *P* < 0.01.

of tumor cell-EC cross-talk that is relevant to tumor formation. Since OSM-signaling functions in only a limited number of tissues (25) and mice with systemic KO of *Osmr* are viable and fertile (10), inhibition of OSM signaling may represent an amenable therapeutic option for ccRCC and other cancers.

The above observations are summarized in the Graphic Abstract. Our discovery demonstrates that microenvironment reconstituted

by the original *VHL* genetic defect in the epithelial cells is a critical factor in ccRCC progression, and provides a useful framework for further elucidation of the molecular and cellular mechanisms involved in this process.

Authors' Disclosures

No disclosures were reported.

Authors' Contributions

H.-H. Nguyen-Tran: Conceptualization, data curation, formal analysis, validation, investigation, visualization, methodology, writing—original draft, writing—review and editing. **T.-N. Nguyen:** Investigation, methodology. **C.-Y. Chen:** Investigation, methodology. **T. Hsu:** Conceptualization, resources, data curation, formal analysis, supervision, funding acquisition, validation, investigation, visualization, methodology, project administration, writing—review and editing.

Acknowledgments

This study was supported by a grant from the National Health Research Institute, Taiwan, ROC (#NHRI-EX108-10801B1), and a grant from the Ministry of Science and Technology, Taiwan, ROC (#MOST 109-2320-B-008-002-MY3). The Hsu

laboratory is also supported by a Chair Professorship of Taiwan Bio-development Foundation. The authors thank the Molecular and Genetic Imaging Center, National Yang-Ming University, Taiwan Animal Consortium, and Center for Advanced Molecular Imaging and Translation, Chang Gung Memorial Hospital, Linkou, Taiwan, for technical support in IVIS experiment.

The costs of publication of this article were defrayed in part by the payment of page charges. This article must therefore be hereby marked *advertisement* in accordance with 18 U.S.C. Section 1734 solely to indicate this fact.

Received February 1, 2021; revised June 22, 2021; accepted July 21, 2021; published first July 23, 2021.

References

- de Vivar Chevez AR, Finke J, Bukowski R. The role of inflammation in kidney cancer. *Adv Exp Med Biol* 2014;816:197–234.
- Diaz-Montero CM, Rini BI, Finke JH. The immunology of renal cell carcinoma. *Nat Rev Nephrol* 2020;16:721–35.
- Greten FR, Grivnickov SI. Inflammation and cancer: triggers, mechanisms, and consequences. *Immunity* 2019;51:27–41.
- Hsu T, Nguyen-Tran HH, Trojanowska M. Active roles of dysfunctional vascular endothelium in fibrosis and cancer. *J Biomed Sci* 2019;26:86.
- Gossage L, Eisen T, Maher ER. VHL, the story of a tumour suppressor gene. *Nat Rev Cancer* 2015;15:55–64.
- Young AC, Craven RA, Cohen D, Taylor C, Booth C, Harnden P, et al. Analysis of VHL gene alterations and their relationship to clinical parameters in sporadic conventional renal cell carcinoma. *Clin Cancer Res* 2009;15:7582–92.
- Kaelin WG Jr. The VHL tumor suppressor gene: insights into oxygen sensing and cancer. *Trans Am Clin Climatol Assoc* 2017;128:298–307.
- Pritchett TL, Bader HL, Henderson J, Hsu T. Conditional inactivation of the mouse von Hippel-Lindau tumor suppressor gene results in wide-spread hyperplastic, inflammatory and fibrotic lesions in the kidney. *Oncogene* 2015;34:2631–9.
- Kuo CY, Lin CH, Hsu T. VHL inactivation in precancerous kidney cells induces an inflammatory response via ER stress-activated IRE1 α signaling. *Cancer Res* 2017;77:3406–16.
- Tanaka M, Hirabayashi Y, Sekiguchi T, Inoue T, Katsuki M, Miyajima A. Targeted disruption of oncostatin M receptor results in altered hematopoiesis. *Blood* 2003;102:3154–62.
- Podgrabinska S, Braun P, Velasco P, Kloos B, Pepper MS, Skobe M. Molecular characterization of lymphatic endothelial cells. *Proc Natl Acad Sci U S A* 2002;99:16069–74.
- Yang Z, Ming XF. Arginase: the emerging therapeutic target for vascular oxidative stress and inflammation. *Front Immunol* 2013;4:149.
- Kovacic JC, Dimmeler S, Harvey RP, Finkel T, Aikawa E, Krenning G, et al. Endothelial to mesenchymal transition in cardiovascular disease: JACC state-of-the-art review. *J Am Coll Cardiol* 2019;73:190–209.
- Ma J, Sanchez-Duffhues G, Goumans MJ, Ten Dijke P. TGF- β -induced endothelial to mesenchymal transition in disease and tissue engineering. *Front Cell Dev Biol* 2020;8:260.
- Ranchoux B, Antigny F, Rucker-Martin C, Hautefort A, Pechoux C, Bogaard HJ, et al. Endothelial-to-mesenchymal transition in pulmonary hypertension. *Circulation* 2015;131:1006–18.
- Sabbisetti VS, Waikar SS, Antoine DJ, Smiles A, Wang C, Ravisankar A, et al. Blood kidney injury molecule-1 is a biomarker of acute and chronic kidney injury and predicts progression to ESRD in type I diabetes. *J Am Soc Nephrol* 2014;25:2177–86.
- Scelo G, Muller DC, Riboli E, Johansson M, Cross AJ, Vineis P, et al. KIM-1 as a blood-based marker for early detection of kidney cancer: a prospective nested case-control study. *Clin Cancer Res* 2018;24:5594–601.
- Moschen AR, Adolph TE, Gerner RR, Wieser V, Tilg H. Lipocalin-2: a master mediator of intestinal and metabolic inflammation. *Trends Endocrinol Metab* 2017;28:388–97.
- Jones SA, Jenkins BJ. Recent insights into targeting the IL-6 cytokine family in inflammatory diseases and cancer. *Nat Rev Immunol* 2018;18:773–89.
- Wang Q, He Z, Huang M, Liu T, Wang Y, Xu H, et al. Vascular niche IL-6 induces alternative macrophage activation in glioblastoma through HIF-2 α . *Nat Commun* 2018;9:559.
- Neiva KG, Warner KA, Campos MS, Zhang Z, Moren J, Danciu TE, et al. Endothelial cell-derived interleukin-6 regulates tumor growth. *BMC Cancer* 2014;14:99.
- Modur V, Feldhaus MJ, Weyrich AS, Jicha DL, Prescott SM, Zimmerman GA, et al. Oncostatin M is a proinflammatory mediator. In vivo effects correlate with endothelial cell expression of inflammatory cytokines and adhesion molecules. *J Clin Invest* 1997;100:158–68.
- Brown TJ, Rowe JM, Liu JW, Shoyab M. Regulation of IL-6 expression by oncostatin M. *J Immunol* 1991;147:2175–80.
- Stawski L, Trojanowska M. Oncostatin M and its role in fibrosis. *Connect Tissue Res* 2018;1–10.
- West NR, Owens BMJ, Hegazy AN. The oncostatin M-stromal cell axis in health and disease. *Scand J Immunol* 2018;88:e12694.
- West NR, Hegazy AN, Owens BMJ, Bullers SJ, Linggi B, Buonocore S, et al. Oncostatin M drives intestinal inflammation and predicts response to tumor necrosis factor-neutralizing therapy in patients with inflammatory bowel disease. *Nat Med* 2017;23:579–89.
- Junk DJ, Bryson BL, Smigiel JM, Parameswaran N, Bartel CA, Jackson MW. Oncostatin M promotes cancer cell plasticity through cooperative STAT3-SMAD3 signaling. *Oncogene* 2017;36:4001–13.
- Lindberg RA, Juan TS, Welcher AA, Sun Y, Cupples R, Guthrie B, et al. Cloning and characterization of a specific receptor for mouse oncostatin M. *Mol Cell Biol* 1998;18:3357–67.
- Linsley PS, Bolton-Hanson M, Horn D, Malik N, Kallestad JC, Ochs V, et al. Identification and characterization of cellular receptors for the growth regulator, oncostatin M. *J Biol Chem* 1989;264:4282–9.
- Tawara K, Bolin C, Koncinsky J, Kadaba S, Covert H, Sutherland C, et al. OSM potentiates preinvasation events, increases CTC counts, and promotes breast cancer metastasis to the lung. *Breast Cancer Res* 2018;20:53.
- Zeisberg EM, Potenta S, Xie L, Zeisberg M, Kalluri R. Discovery of endothelial to mesenchymal transition as a source for carcinoma-associated fibroblasts. *Cancer Res* 2007;67:10123–8.
- Mauer J, Chaurasia B, Goldau J, Vogt MC, Ruud J, Nguyen KD, et al. Signaling by IL-6 promotes alternative activation of macrophages to limit endotoxemia and obesity-associated resistance to insulin. *Nat Immunol* 2014;15:423–30.
- Piera-Velazquez S, Mendoza FA, Jimenez SA. Endothelial to mesenchymal transition (EndoMT) in the pathogenesis of human fibrotic diseases. *J Clin Med* 2016;5:45.
- Smigiel JM, Parameswaran N, Jackson MW. Potent EMT and CSC phenotypes are induced by oncostatin-M in pancreatic cancer. *Mol Cancer Res* 2017;15:478–88.